Strain visualization of growing short fatigue cracks in the heat-affected zone of a Ni–Cr–Mo–V steel welded joint: Intergranular cracking and crack closure

Shi-Dong Liu[a], Ming-Liang Zhu[a,*], Hai-Bo Zhou[b], Di Wan[c], Fu-Zhen Xuan[a]

a. Key Laboratory of Pressure Systems and Safety, Ministry of Education; School of Mechanical and Power Engineering, East China University of Science and Technology, Shanghai 200237, China

b. State Key Laboratory of High Performance Complex Manufacturing, Central South University, Changsha 12570, China

c. Department of Mechanical and Industrial Engineering, Norwegian University of Science and Technology, Richard Birkelands Vei 2B, 7491 Trondheim, Norway

Tel: 86-21-64253776; Fax: 86-21-64253513. E-mail: mlzhu@ecust.edu.cn

Abstract

Physically short fatigue crack growth behavior in the heat-affected zone of a Ni–Cr–Mo–V steel welded joint was investigated in-situ in SEM to reveal effects of crack closure and tortuous crack growth path on crack-tip straining behavior with the help of high resolution digital image correlation technique. The crack growth path and associated fatigue damage at microstructural scale was characterized by electron backscatter diffraction and electron channeling contrast imaging techniques. Results showed that the short crack growth was influenced by both local microstructure and global strength gradient. The short crack could deflect intergranularly when meeting with one large grain due to misfit deformation and strain localization. The crack closure, which was accompanied during loading and unloading in terms of crack surface contact, shielded the real crack-tip and manifested itself well in both compressive strain at crack wake and strain development at crack-tip. It is indicated that strain localization at lathy boundaries and formation of sub-grains was responsible for the fatigue of short cracks.

Keywords: Short fatigue crack; Crack closure; Crack deflection; Intergranular cracking;

* Corresponding author.

Digital image correlation; Strain localization

1. Introduction

The growth of short crack under cyclic loading, as the most life-consuming stage in total fatigue life of engineering materials and structures, has been widely investigated since the 1980s [1]. It is generally believed that short fatigue cracks are more susceptible to local microstructures [2], grain boundaries [3], orientation of grains [4], and crack closure [5]. The growth of short cracks is more often coupled with material damage and localized plasticity, while the traditional linear elastic fracture mechanics is not a proper tool for characterizing the propagation behavior [5,6]. The situation becomes more complex when a short crack initiates from welded defects such as porosity and lack of penetration [7,8], and grows within a narrow heat-affected zone (HAZ) of a welded joint. The understanding of cracking behavior within the HAZ of welded joint is critical in structural integrity assessment [8,9], and both the influences of local microstructures [10] and strength gradient [11] in HAZ need to be considered.

The distribution of strains at crack-tip seems to be the key to understanding fatigue cracking process [[12], [13], [14]]. Digital Image Correlation (DIC) technique has been widely used to track the strain maps during the specimen loading [15,16]. It has been utilized for strain field characterization of both static [17,18] and growing fatigue cracks [19,20], and the influence of overload [21,22]. The finding of ratchetting at crack-tip by Zhu et al. [19] and Carroll et al. [23] provides the basis on how fatigue crack grows, and is helpful to develop the criterion of fatigue cracking in terms of strain [19,24]. Based on in-situ loading and crack growth path characterization, Zhu et al. [25] reported the development of crack closure during the growth of short cracks, while the influence

of crack closure on crack-tip straining has not fully been illustrated up to now, although the effective stress intensity approach has long been developed in 1970s by Elber [26]. In addition, current investigations of strain characterization focus mainly on ideal and stable growing cracks rather than the growing crack with a tortuous path when encountering barriers or is driven by additional strength gradient. The strain approach to driving force of micro-cracking and short crack growth would be more convincing if the mode of fatigue crack growth had been taken into account.

It is known that characterization of strain localization and associated fatigue damage at microstructural scale is beneficial to understand variations of fatigue crack growth rate and crack path. Carroll et al. [23] reported the strain was localized at slip bands within grains and on twin and grain boundaries by linking the strain measurements with electron backscatter diffraction (EBSD). It seems the technique of electron channeling contrast imaging (ECCI) [27,28] is helpful to provide information on grain size of polycrystalline materials, local crystal distortions, and dislocations with a larger area of view based on the contrast resulted from the channeling effect. This technique, when combined with EBSD [29,30], would present a full view of local microstructural damage under cyclic loadings, and thus underpin a mechanistic understanding of short crack growth behavior.

Therefore, in the present work, the short crack growth and its microstructure influences in the narrow HAZ were characterized based on in-situ SEM and DIC techniques. The governing factors for the growing short crack and associated crack closure effect on near-tip straining were assessed based on the strain approach, while

microstructural damage accompanying crack extension was also highlighted.

2. Materials and experimental methods

2.1 Materials

The materials employed in this investigation were welded joint of NiCrMoV rotor steel, which was welded by submerged arc welding technique. The current research is focused on the HAZ of the welds. The chemical composition of base metal in wt.% includes Ni 3.56, Cr 1.71, Mo 0.38, Mn 0.29, V 0.09, C 0.25, and Fe is the balance. The welds were undergone a post weld heat treatment as well as an artificial thermal ageing at 350 °C for 3000 h. The HAZ can be divided into three subzones, i.e., fully quenched-tempered zone (FQTZ), partially quenched-tempered zone (PQTZ) and tempered zone (TZ) [25,[31], [32], [33]]. As shown in Fig. 1, the microstructures in the FQTZ mainly include tempered martensites and bainites, with many fine precipitates both in and around the boundaries of lathy martensites (Fig. 1a and b). The prior austenite grain size in the FQTZ is around 60 μm. The microstructures illustrated by transmission electron microscope (TEM) in Fig. 1 (c) indicate dislocations as well as precipitates. The microstructures have been reported in an independent paper in Chinese [34]. A full coverage of microstructure variations before and after the aging process has been reported in our previous work [25], and was correlated with tensile behavior based on miniature sample testing. Another previous work on observation and modeling of short crack closure was reported in Ref. [25], where the crack closure level at the crack wake was measured based on imaging analysis.

2.2 In situ fatigue crack growth tests

Fig. 2 shows the shape and dimensions of specimens for in-situ fatigue crack growth tests. The single edge notch tension (SENT) miniature specimen with a short crack length of approximately 0.5 mm and a thickness of 0.5 mm, was cut from a larger three-point single edge notch bending (SENB) specimen with an initial notch at the FQTZ (with a yield strength σ_y of 646 MPa). The SENB specimen, with a thickness of 8 mm, a width of 16 mm, an initial notch length of 1.7 mm, and a distance to the fusion line of 0.19 mm, was pre-cracked under cyclic loadings (load ratio of 0.1) on high frequency testing machine under a frequency around 90 Hz [25]. The stress intensity factor (SIF) range, ΔK, during the pre-cracking process was increased from 11.9 MPa $m^{1/2}$ to 12.4 MPa $m^{1/2}$ for a first fatigue crack extension of 0.5 mm, followed by another 5% load decrease for another 0.5 mm extension, the final ΔK after pre-cracking was 17.85 MPa $m^{1/2}$. In total, the pre-crack length was 1 mm. The SIF is calculated based on Eqs. (1), (2), (3) according to ISO 12108. After pre-cracking, the cyclic plastic zone size at crack-tip of the SENB specimen was estimated as 20 μm, according to Irwin's model under plane strain state, $r_c=(1/12\pi)\cdot(\Delta K/\sigma_y)^2$. It is expected that the in-situ fatigue test with very thin specimen will be less influenced by pre-cracking as residual stresses have been relaxed during machining process.

$$K = \frac{F}{BW^{0.5}} g\left(\frac{a}{W}\right) \quad (1)$$

where the α is defined as the ratio of a to W. The $g(a/W)$ of SENB and SENT specimens are calculated by Eqs. (2), (3).

$$g\left(\frac{a}{W}\right) = \frac{6\alpha^{0.5}}{[(1-2\alpha)(1-\alpha)^{1.5}]}[1.99 - \alpha(1-\alpha)(2.15 - 3.93\alpha + 2.7\alpha^2)] \quad (2)$$

The $g(a/W)$ of SENT specimen is calculated by

$$g\left(\frac{a}{W}\right) = (1-\alpha)^{-1.5}(1.9878\alpha^{0.5} - 2.9726\alpha^{1.5} + 6.9503\alpha^{2.5} - 14.4476\alpha^{3.5} + 10.0548\alpha^{4.5} + 3.4047\alpha^{5.5} - 8.7143\alpha^{6.5} + 3.7417\alpha^{7.5}) \quad (3)$$

The thickness of the SENT specimen is less than $2.5(K_{max}/\sigma_y)^2$, where the K_{max} is the maximum SIF, indicating a plane stress dominant state throughout the crack growth process. This also implies the insignificant effect of pre-cracking on fatigue crack growth using the miniature samples. To assure the pre-crack in the regime of physically short crack, the cyclic plastic zone size is approximately limited to one-tenth of the crack length according to Irwin's model [4,35,36] under plane stress condition, $r_c=(1/4\pi) \cdot (\Delta K/\sigma_y)^2$. The linear elastic fracture mechanics (LEFM) was thus employed to calculate ΔK of the physically short crack growth.

Prior to fatigue test, all specimens were polished and etched before being mounted onto the in-situ loading stage equipped in SEM. The loading stage (Deben Co. Ltd, UK) had a capacity of 2 kN and was working under displacement control mode. Cyclic loading at a load ratio of 0.1 in triangular waveform was exerted on the miniature specimen with a frequency of 0.06 Hz, under a high vacuum environment at room temperature. The crack-tip area was real-time monitored and tests were interrupted for taking high resolution images. Two specimens were tested, with one of them having short crack extension while the other one having longer extension and tortuous advancing path, indicating strong local microstructure influences. Crack closure behavior was investigated by analyzing a series of images within a full loading cycle.

2.3 Digital image correlation

The DIC technique was used to obtain full field displacement and strain distribution by comparing two images with different deformation. The in-plane strain was analyzed by commercial DIC software (VIC-2D 2009, Correlated Solutions, USA) with intrinsic microstructures as speckle pattern. According to the algorithm, the full field strain distribution near crack-tip was measured by choosing one reference image and several deformed images, with suitable interpolation. The subset size and step size are important parameters during the correlation, which needs careful error analysis as reported in Ref. [37]. In this work, the images with size of 1024 × 768 pixels, and thus a pixel size (resolution) of 54 nm/pixel was achieved. The subset size and step size were chosen as 21 pixels and 5 pixels, respectively, which has sufficient resolution for near-tip strain measurement [37].

2.4 Fatigue damage characterization

After the fatigue test, the microstructures around the crack-tip and along crack path were observed by EBSD and ECCI techniques. The specimens were mechanically polished using colloidal silica for 30 min. ECCI and EBSD observations were performed using a backscattered electron (BSE) detector mounted on a SEM (TESCAN MIRA3, Czech Republic). The EBSD measurement was carried out at a step size of 0.2 μm and a voltage of 20 kV while ECCI observation was performed at 10 kV.

3. Results

3.1 Short crack growth behavior

Fig. 3 presents the a-N relationship and da/dN-ΔK relationship of the growth behavior of physically short cracks in the two miniature specimens, as reported in the Chinese paper [34]. Note the x-axis is in logarithmic scale. The specimen No.1 has a short growth length of 32.7 μm while crack in specimen No.2 grows for about 98 μm, and the

specimen No.1 was tested at a higher stress level [25]. The *a*-*N* data points tend to merge with each other, indicating good repeatability of the in-situ fatigue tests. Nevertheless, the crack growth data show a fluctuating pattern, which is related to a short extension between two data points due to interruption of crack growth test for taking images. The fluctuation of d*a*/d*N* also implies the strong influence of local microstructures. The d*a*/d*N* is in the range of 1×10^{-5} mm/cycle and 7×10^{-5} mm/cycle. It is interesting to find that the d*a*/d*N* of specimen No.2 decreases firstly and finally tends to merge with the data of specimen No.1 when ΔK is higher than 18.5 MPa $m^{1/2}$. Meanwhile, the specimen No.2 undergoes more serious fluctuations than specimen No.1, indicating a stress level dependence, i.e., higher stress level with lower fluctuations, which seems to be consistent with the results by McDowell and Bennett [38], and Lopez-Crespo et al. [39].

3.2 Crack growth morphologies

The morphologies of short crack growth path of specimen No.1 at maximum load, Pmax, are illustrated in Fig. 4. The short crack has a total growth length of 24.2 μm within 611 cycles. The growing fatigue crack has to overcome densely distributed local lathy martensites, a process which results in local tortuous advancing of fatigue crack. It is also observed that the growing main crack has a tendency to deflect downward due to the gradient strength distribution in the HAZ. Note the hardness and strength in HAZ decline gradually from the fusion line to the base material [32,40]. It appears that the short crack growth behavior within the FQTZ is affected by local microstructures as well as the globe strength gradient.

Fig. 5 shows the crack growth path in specimen No.2. It is observed that the crack deflects at first when meeting a large grain (Fig. 5a–c) and then grows intergranularly after deviating towards the main crack growth direction (Fig. 5d and e). This implies a strong influence of local microstructures on short crack growth. Meanwhile, the growth rate of crack slows down at this stage, which indicates that the short fatigue crack can choose a favorable way to extend, and the growth direction is vulnerable to local obstacles, i.e., a large grain in front of crack-tip. Note that the crack growth length is calculated along the central plane of the loading. The cracking mechanisms and associated near-tip strain evolution will be discussed later.

3.3 Observation of crack closure in a full cycle

During the measurement of crack closure, a few more cycles were conducted manually to identify where the crack was fully closed, and thus to identify the stress level corresponding to crack closure. In a full loading cycle, SEM images with high magnification were taken at selected load levels in the range from P_{min} to P_{max} with the ratio of P/P_{max} increasing (or decreasing) at an increment (or decrement) of 0.1. Fig. 6 shows the morphologies of crack growth path in the full loading-unloading cycle at a ΔK of 19.45 MPa $m^{1/2}$. It is observed that during the loading part, there is at least a length of 9 μm behind the crack-tip is not open when the current load level is as high as 40% of P_{max}, $P/P_{max} = 0.4$. This agrees well with the closure behavior observed in the unloading part in Fig. 6e. Similarly, a crack length of 14 μm behind the crack-tip is not open or closed during the loading and unloading process at $P/P_{max} = 0.2$. For the closed crack, the fracture surfaces have direct contact with each other. Any implications of

crack wake contact in the strain evolution at crack-tip will be discussed later.

4. Discussion

4.1 Full field strain and plastic zone for stable crack growth

Fig. 7 shows the evolution of crack-tip strain and variation of size and shape of plastic zone during the short crack extension period. Such kind of crack growth is relatively stable as the crack path is not as tortuous as that of in specimen No.2. Note that the strain distribution was calculated by taking the first image at minimum loading at N of 458 cycles as reference while those images at maximum loading levels as deformed. As a result, the normal strain component, ε_{yy}, actually represents strain range value. A bean-shaped highly strained zone can be observed near crack-tip, which is believed to be the plastic zone. With extension of the short crack, the size of the highly strained zone does not change significantly while the shape of such zones can vary a lot. A smaller change of crack-tip direction seems to have a big influence on the strained zone. This implies the influence of local microstructures which controls the pattern the short crack grows. It is noteworthy that the lower part of highly strained zone stretches more widely in case the crack shows a downward growing due to local strength gradient within the HAZ, as illustrated by the arrows in Fig. 7a. This indicates that the global gradient strength distribution acts like an added driving force for local crack growth behavior and results in asymmetric deformation near crack-tip. The strain at the wake of crack-tip is mainly in tension which accords with the concept of plasticity-induced crack closure proposed by Elber [26,41], who attributed the occurrence of fracture surface contact to plastic deformation in the wake of a growing crack. The permanent tensile

plastic deformation at crack wake was also reported by Zhao et al. [42] based on a detailed elastic-plastic finite element analysis.

It is also interesting to find that a local compressive straining zone at the wake of growing short fatigue crack is gradually developed. The longer the crack extends, the larger the size of compressive zone, and during this process, the plastic zone in front of crack-tip reduces accordingly. It is worth noting that the local compressive strain field is located in the region where the crack path is more seriously deflected and enlarged with crack extension, which seems to be related to the development of roughness-induced crack closure. Roughness-induced crack closure is associated with misfit of deformation at microstructural inhomogeneity, resulting in local displacement in the crack propagation direction or out-of-plane displacement due to local mode II or III deformation [43]. Pippan et al. [44] concluded that the asymmetric arrangement of geometrically necessary dislocations leaded to an asymmetric displacement, and induced an asymmetric change of crystal orientation between the two crack flanks. In this work, the local compressive strain within a global tensile strain denotes the misfit of deformation at microstructural scale as a result of high resolution DIC and implies the possibility of drastic microstructure damage at local areas. The microstructural damage analysis based on EBSD technique will be discussed later.

Fig. 8 illustrates quantitatively the evolution of compressive strain zone at crack wake and plastic zone at crack-tip. In this work, a miniature smooth specimen was loaded in tension until the yielding was determined at the point of F, as shown in Fig. 8a. In this process, a series of SEM images were taken during the interruption periods for strain

measurement. Note that the image magnifications and area of interest are the same as in Fig. 7. Images taken at the yielding point were then correlated with those at zero load based on the DIC technique. It is observed that an average strain at the corresponding point F is 1.79%, which represents the plastic strain value when the HAZ is undergoing plastic deformation. This threshold value for plastic deformation was then input into the strain distribution in Fig. 7, as a result, the evolution of plastic zone area at crack-tip as opposite to the compressive straining area at crack wake was determined as shown in Fig. 8b. It is obvious there is a gradual increase of compressive straining area from 300 to 850 μm^2 and a slow decrease of plastic zone area at crack-tip from 750 to 600 μm^2, which provides direct evidence for the effect of roughness-induced crack closure on crack-tip straining during crack extension.

4.2 Strain evolution during deflection of crack growth path

Fig. 9 illustrates the variation of normal and shear strain distribution when the crack deflects towards the large grain, during which the loading mode of fatigue cracking alternates. The crack is starting to grow upward in Fig. 9a and d, where the normal strain dominates crack growth with tensile deformation at crack-tip and the shear strain is compressive. The crack in Fig. 9b and e is pure mode II like, a case where the plastic zone at crack-tip is asymmetrical relative to external loading direction, and it seems the compressive shear strain localized at the crack-tip is driving crack growth upward. The cracks in Fig. 9c and f show a mixed I/II mode, where the highly strained zone returns to crack-tip with asymmetrical plastic zone while shear strain is also active. With the deflection of fatigue crack growth path, the distribution of strains changes and the

dominant strain (normal or shear) for crack growth varies accordingly. The normal strain provides the contribution of mode I tensile deformation in crack growth while the shear strain implies shear deformation between crack surfaces. The deflection of crack growth path which is associated with misfit deformation and asymmetric crack wake plasticity, and thus contributes to the development of roughness-induced crack closure [44].

4.3 Strain evolution during intergranular cracking

Fig. 10 illustrates the strain evolution of the crack growing along one grain boundary after deflection. It is obvious that the normal strain distribution at crack-tip varies significantly with intergranular crack growth and the bean-shaped plastic zone vanishes due to asymmetric deformation. The evolution of crack-tip strain is also related with a misfit of deformation within and out of the grain due to inhomogeneous microstructures. The strain localization at crack-tip in Fig. 10a accords well with the following crack growth path along grain boundary, as observed in Fig. 10b. This indicates intergranular cracking is associated with strain localization at preferential crack growth path. The intergranular cracking is thus also helpful to the development of roughness-induced crack closure. As a result, the deflection of crack growth path and intergranular cracking contribute to the full evolution of crack closure during crack growth of the physically short crack, based on the experimental measurement of crack closure level in our previous work [25]. As for the shear strain, it is observed that the deformation below the crack plane is always positive while the upper side is negative, which implies strong misfit deformation during intergranular cracking. As shown in Fig. 10, it is inferred that

the positive shear strain may be related to the direction of crack growth path as the final crack path tends to deviate to the mid-plane recovering the pure mode I of cracking. It would be interesting to monitor the evolution of shear strain at the particular point with the number of cycles where its driving force role can be verified experimentally.

4.4 Strain evolution in case of crack closure

Fig. 11 shows the evolution of full field strain within a loading-unloading cycle. Note the calculated strain distribution was based on correlations relative to the minimum load, P_{min}. A full mask of crack wake (did not participate in strain correlation in DIC) was employed during the correlation, as a result, the correlation illustrates straining behavior at the real crack-tip. An observable strain field is developed at the crack-tip when P/P_{max} reaches 0.4 at which the crack is undergoing partial closure with a length of 9 μm (Fig. 6b). Interestingly, there is no obvious strain concentration at P/P_{max} of 0.2 at which the closed crack length is 14 μm (Fig. 6a). With the increase of P/P_{max} to 0.7, the plastic zone develops, and continues to enlarge into its final form at the maximum load. In the unloading process, it is observed that the strain concentration area at the crack-tip is almost disappeared when the load decreases to $0.4P_{max}$, which is probably due to a relaxation of residual stress, resulting in a more dispersed strain distribution pattern in Fig. 11e. It is believed that the external load for P/P_{max} in the range of 0.1–0.4 has little contribution to crack-tip straining and is mainly used to open the partial closed crack. It is thus concluded that the crack closure at crack wake has a great influence on the strain field evolution at crack-tip. The question remains on how the crack surface contact affects the strain localization at real crack-tip.

A verification of strain evolution and associated strain transfer in case of crack closure was carried out by strain correlation using instant crack-tip, as the closed crack length is known beforehand as shown in Fig. 6. In this case, only the known open crack wake was masked during the strain correlation, and thus the closed part of crack path was participated in DIC calculation. More specifically, the strain calculation in DIC in this case was carried out by ignoring the open crack path and taking the closed part into account. As shown in Fig. 12, no obvious strain accumulation below P/P_{max} of 0.2 is observed at the instant crack-tip, nevertheless, the strain accumulation has occurred at P/P_{max} of 0.4 (both loading and unloading) in the closed part of crack-tip where most of the higher straining zone is located around the closed crack path, indicating the closed part and its neighborhood has localized straining. In this case, the plastic zone at the real crack-tip is not fully developed. This is different from the case reported in Fig. 11. Such kind of strain localization has implied the shielding effect of real crack-tip for plastic deformation in the case of crack closure, and the crack surface has physical contact with each other. It is therefore concluded that the crack closure occurred at crack wake has affected the straining at crack-tip. This seems to be the first time to report the inter-relationship between crack closure and crack-tip straining.

4.5 Quantitative distribution of strain and COD values

Fig. 13 illustrates the quantitative distribution of strain field in front of the crack-tip and crack opening displacement at the crack wake in a complete loading-unloading cycle at a similar ΔK of Fig. 11, Fig. 12. Note the strain values are selected at 2 μm, 5 μm and 10 μm in front of the crack-tip along the x axis of a local co-ordinate system, while the

COD values are distracted at 5 μm, 10 μm and 20 μm behind the crack-tip, as shown in Fig. 13a. An almost linear relationship between P/P_{max} and ε_{yy} is observed in Fig. 13b in case of the distance is 10 μm, which indicates little influence of near crack-tip plasticity on the mechanical response. As for strains close to the crack-tip, strain values are enhanced and there is a "knee" for P/P_{max} around 0.4 where nonlinearities occur due to local plasticity. Interestingly, during the unloading process, the nonlinearities occur a little bit later at a P/P_{max} around 0.3, implying residual strains. Such kind of "knee" is also apparent in Fig. 13c where the COD values deviate from an initial linear relationship, and the crack closure level is estimated at P/P_{max} between 0.3 and 0.4. The evolution of COD is consistent with both experimental and numerical results reported in Refs. [45,46]. As a result, the crack closure level determination based on COD variation at crack wake and near-tip strain evolution is consistent with that observed from surface morphologies in Fig. 6. The similar patterns for COD and strain within a full cycle in the near crack-tip zone imply an almost simultaneous mechanical response for crack opening/closure and straining. It is reasonable to conclude that the crack surface contact is helpful to load transfer between crack wake and crack-tip, and the closed part acts like a "bridge".

4.6 Damage characterization along the crack propagation path

Fig. 14 shows a group of images from ECCI observation of crack growth path of specimen No.1. A step-by-step magnification of views present the deformation structure along the crack path. The martensite laths can be clearly observed with deformation structure inside. Interestingly, the crack has been propagating along the lath boundaries,

as clearly recorded in Fig. 14c. The deformation structure along the crack path is mainly presented as dislocation cells, as indicated in Fig. 14c, which tend to form low angle grain boundary and sub-grain structures. This indicates a relatively severe plastic deformation in this region, in agreement with the crack-tip final fracture zone. In comparison with the initial microstructures investigated by TEM (Fig. 1c), the deformation structures in Fig. 14 shows a higher dislocation density. The formation of dislocation cell structure is reasonable. It is known that during plastic loading, the initial dislocations with high density will try to form organized structures according to the crystallography and loading conditions during plastic loading, while dislocations annihilate with each other during unloading. However, some dislocations do not behave in the same way during unloading, and may be "pinned" at some places. After some cycles, they accumulate and form boundary-like structures, which can act as damage initiation sites in the further loading steps.

Fig. 15 shows EBSD morphologies of the two specimens at crack-tip and along the deflected crack path. The inverse pole figure (IPF) maps are shown in Fig. 15a and b. Both Figs. 15a and b show how the fatigue crack has been propagating at the particular stage, where the fatigue crack alternates its path along the lathy boundaries and passes through the laths perpendicularly. One advantage of the EBSD observation is the ability to show the distribution of crystal orientation. It is obvious in Fig. 15a that the orientation varies accordingly with the extension of crack growth, and there is less variation of orientation close to the crack-tip. This is mainly due to the crack growth is relatively stable with slight path deflection near crack-tip. It is worth noting that one

block of lathy martensites in the middle of Fig. 15a differs strongly with its nearby microstructures by orientation. As reported in Ref. [43], the change of the color is a measure for the orientation change, that is, lattice rotation. It is thus inferred that the local microstructures may have undergone a different deformation mode, most probably the occurrence of lattice rotation. If it were, then it would help explain the compressive straining at the crack wake, as reported in Fig. 7 and quantitatively assessed in Fig. 8. Interestingly, the color difference and thus crystal orientation in Fig. 15b show strong heterogeneity, which implies significant plastic deformation during crack path deflection. It is inferred that in case of mixed mode crack growth, the dominant shear deformation has resulted in microstructural damage different from that of pure mode I deformation.

Furthermore, the kernel average mis-orientation (KAM) maps are used to indicate the local straining level in Fig. 16. In Fig. 16, the boundaries of large angle grains (15–60°) are marked with black lines, and the label from 0 to 5 shows severity of inhomogeneous deformation at microstructural scale. In this work, the highest level of 5 in strong red color denotes the small angle grains (2–15°). It is observed once again that the plastic deformation is mainly accumulated at martensitic lath boundaries. Combining the ECCI analysis in Fig. 14, it can be inferred that the strain localization at the lath boundaries can possibly promote the formation of sub-grain boundaries and contribute to deformation incompatibilities during loading. This incompatibility can be a sensitive and weak spot for the fatigue damage accumulation and crack propagation that can lead to the deflection of the crack growth path. This seems to be the origin of the

microstructural influence of the crack growth behavior.

5. Conclusions

In this work, the effects of crack closure and tortuous crack grow path on crack-tip straining behavior was investigated based on in-situ SEM/DIC technique. The crack growth path and associated fatigue damage at microstructural scale was characterized by both EBSD and ECCI techniques. The main conclusions are listed as follows.

(1) The short fatigue crack growth within the HAZ of the welded joint often shows a deflected crack growth path due to the combined contribution of local microstructures and global strength gradient.

(2) A deflection of growing crack path as well as intergranular cracking manifests itself well in terms of crack-tip straining and its localization where the normal and shear strains dominate alternatively in the case of cracking mode changes.

(3) The crack closure was evidenced by direct crack path observation, COD/crack-tip strain measurement, and the gradual development of compressive residual strain at crack wake, which is believed to shield the real crack-tip and thus affect strain field in front of crack-tip.

(4) The short fatigue crack propagation behavior can correlate well with fatigue damage at microstructural scale, in which the strain tends to localize at lathy boundaries, promoting deformation incompatibility and formation of sub-grains.

Declaration of competing interest

We declare that we do not have any commercial or associative interest that represents a conflict of interest in connection with the work submitted.

Acknowledgements

The authors are grateful for the supports provided by the National Natural Science Foundation of China (51575182, 51835003), and the Open Research Fund of Key Laboratory of High Performance Complex Manufacturing, Central South University (Kfkt2016-13).

References

[1]
K.J. Miller
The behaviour of short fatigue cracks and their initiation part II-a general summary
Fatigue Fract. Eng. Mater. Struct., 10 (2) (1987), pp. 93-113
[2]
P.D. Nezhadfar, E. Burford, K. Anderson-Wedge, B. Zhang, S. Shao, S.R. Daniewicz, N. Shamsaei
Fatigue crack growth behavior of additively manufactured 17-4 PH stainless steel: effects of build orientation and microstructure
Int. J. Fatigue, 123 (2019), pp. 168-179
[3]
W. Ludwig, J.Y. Buffiere, S. Savelli, P. Cloetens
Study of the interaction of a short fatigue crack with grain boundaries in a cast Al alloy using X-ray microtomography
Acta Mater., 51 (3) (2003), pp. 585-598
[4]
S. Suresh, R.O. Ritchie
Propagation of short fatigue cracks
Int. Met. Rev., 29 (1) (1984), pp. 445-475
[5]
A.J. Mcevily, D. Eifler, E. Macherauch
An analysis of the growth of short fatigue cracks
Eng. Fract. Mech., 40 (3) (1991), pp. 571-584
[6]
K. Hussain
Short fatigue crack behaviour and analytical models: a review
Eng. Fract. Mech., 58 (4) (1997), pp. 327-354
[7]
S.V. Adiban, M. Ramu
Study on the effect of weld defects on fatigue life of structures
Mater. Today: Proceedings, 5 (9, Part 1) (2018), pp. 17114-17124
[8]

W. Shen, Y. Qiu, L. Xu, L. Song
Stress concentration effect of thin plate joints considering welding defects
Ocean. Eng., 184 (2019), pp. 273-288
[9]
Y. Zhang, D. You, X. Gao, N. Zhang, P.P. Gao
Welding defects detection based on deep learning with multiple optical sensors during disk laser welding of thick plates
J. Manuf. Syst., 51 (2019), pp. 87-94
[10]
W. Wang, T.G. Liu, X.Y. Cao, Y.H. Lu, T. Shoji
In-situ SEM study of crack initiation and propagation behavior in a dissimilar metal welded joint
Mater. Sci. Eng. Struct. Mater. Prop. Microstruct. Process., 729 (2018), pp. 331-339
[11]
R.A. Smith
On the short crack limitations of fracture mechanics
Int. J. Fract., 13 (13) (1977), pp. 717-720
[12]
T.C. Chu, W.F. Ranson, M.A. Sutton
Applications of digital-image-correlation techniques to experimental mechanics
Exp. Mech., 25 (3) (1985), pp. 232-244
[13]
L.L. Zheng, Y.F. Gao, S.Y. Lee, R.I. Barabash, J.H. Lee, P.K. Liaw
Intergranular strain evolution near fatigue crack tips in polycrystalline metals
J. Mech. Phys. Solids, 59 (11) (2011), pp. 2307-2322
[14]
E. Ferrie, M. Sauzay
Influence of local crystallographic orientation on short crack propagation in high cycle fatigue of 316LN steel
J. Nucl. Mater., 386–388 (2009), pp. 666-669
[15]
V. Herrera-Solaz, L. Patriarca, S. Foletti, J. Segurado, M. Niffenegger
Microstructure-based modelling and Digital Image Correlation measurement of strain fields in austenitic stainless steel 316L during tension loading
Mater. Sci. Eng. A, 751 (2019), pp. 99-106
[16]
C.M. Stewart, E. Garcia
Fatigue crack growth of a hot mix asphalt using digital image correlation
Int. J. Fatigue, 120 (2019), pp. 254-266
[17]
J. Tong, B. Lin, Y.W. Lu, K. Madi, Y.H. Tai, J.R. Yates, V. Doquet
Near-tip strain evolution under cyclic loading: in situ experimental observation and numerical modelling
Int. J. Fatigue, 71 (2015), pp. 45-52

[18]
Y.-W. Lu, C. Lupton, M.-L. Zhu, J. Tong
In situ experimental study of near-tip strain evolution of fatigue cracks
Exp. Mech., 55 (6) (2015), pp. 1175-1185
[19]
M.L. Zhu, Y.W. Lu, C. Lupton, J. Tong
In situ near-tip normal strain evolution of a growing fatigue crack
Fatigue Fract. Eng. Mater. Struct., 39 (8) (2016), pp. 950-955
[20]
C. Evans, R. Leiva-Garcia, R. Akid
Strain evolution around corrosion pits under fatigue loading
Theor. Appl. Fract. Mech., 95 (2018), pp. 253-260
[21]
D.-Q. Wang, M.-L. Zhu, F.-Z. Xuan, J. Tong
Crack tip strain evolution and crack closure during overload of a growing fatigue crack
Fract. Struct. Integr., 41 (2017), pp. 143-148
[22]
M. Thielen, F. Schaefer, P. Gruenewald, M. Laub, M. Marx, M. Meixner, M. Klaus, C. Motz
In situ synchrotron stress mappings to characterize overload effects in fatigue crack growth
Int. J. Fatigue, 121 (2019), pp. 155-162
[23]
J.D. Carroll, W. Abuzaid, J. Lambros, H. Sehitoglu
High resolution digital image correlation measurements of strain accumulation in fatigue crack growth
Int. J. Fatigue, 57 (2013), pp. 140-150
[24]
J. Tong, L.G. Zhao, B. Lin
Ratchetting strain as a driving force for fatigue crack growth
Int. J. Fatigue, 46 (2013), pp. 49-57
[25]
M.-L. Zhu, F.-Z. Xuan, S.-T. Tu
Observation and modeling of physically short fatigue crack closure in terms of in-situ SEM fatigue test
Mater. Sci. Eng. A, 618 (0) (2014), pp. 86-95
[26]
W. Elber
M.S. Rosenfeld (Ed.), The Significance of Fatigue Crack Closure, ASTM International, West Conshohocken, PA (1971), pp. 230-242
[27]
K. Habib, M. Koyama, T. Tsuchiyama, H. Noguchi
ECCI characterization of dislocation structures at a non-propagating fatigue crack tip: toward understanding the effects of Mn-C and Cr-N couples on crack growth resistance

Metall. Mater. Trans. A, 50 (1) (2019), pp. 426-435
[28]
S. Han, P. Eisenlohr, M.A. Crimp
ECCI based characterization of dislocation shear in polycrystalline arrays during heterogeneous deformation of commercially pure titanium
Mater. Char., 142 (2018), pp. 504-514
[29]
M.W. Tofique, J. Bergström, K. Svensson, S. Johansson, R.L. Peng
ECCI/EBSD and TEM analysis of plastic fatigue damage accumulation responsible for fatigue crack initiation and propagation in VHCF of duplex stainless steels
Int. J. Fatigue, 100 (2017), pp. 251-262
[30]
B.A. Simkin, B.C. Ng, T.R. Bieler, M.A. Crimp, D.E. Mason
Orientation determination and defect analysis in the near-cubic intermetallic γ-TiAl using SACP, ECCI, and EBSD
Intermetallics, 11 (3) (2003), pp. 215-223
[31]
M.-L. Zhu, F.-Z. Xuan
Effects of temperature on tensile and impact behavior of dissimilar welds of rotor steels
Mater. Des., 31 (7) (2010), pp. 3346-3352
[32]
M.-L. Zhu, F.-Z. Xuan
Correlation between microstructure, hardness and strength in HAZ of dissimilar welds of rotor steels
Mater. Sci. Eng. A, 527 (16–17) (2010), pp. 4035-4042
[33]
M.-L. Zhu, F.-Z. Xuan
Effect of microstructure on strain hardening and strength distributions along a Cr–Ni–Mo–V steel welded joint
Mater. Des., 65 (0) (2015), pp. 707-715
[34]
D. Wang, M. Zhu, F. Xuan
Closure and Crack-Tip Plasticity of Short Fatigue Growing Cracks
(2016)
Sciencepaper Online
http://www.paper.edu.cn/releasepaper/content/201605-1503
[35]
R.O. Ritchie, J. Lankford
Small fatigue cracks: a statement of the problem and potential solutions
Mater. Sci. Eng., 84 (none) (1986), pp. 11-16
[36]
R.C. Mcclung
Crack closure and plastic zone size in fatigue
Fatigue Fract. Eng. Mater. Struct., 14 (4) (2010), pp. 455-468

[37]
D.-Q. Wang, M.-L. Zhu, F.-Z. Xuan
Correlation of local strain with microstructures around fusion zone of a Cr-Ni-Mo-V steel welded joint
Mater. Sci. Eng. A, 685 (2017), pp. 205-212
[38]
D.L. Mcdowell, V.P. Bennett
A microcrack growth law for multiaxial fatigue
Fatigue Fract. Eng. Mater. Struct., 19 (7) (2010), pp. 821-837
[39]
P. Lopez-Crespo, A. Garcia-Gonzalez, B. Moreno, A. Lopez-Moreno, J. Zapatero
Some observations on short fatigue cracks under biaxial fatigue
Theor. Appl. Fract. Mech., 80 (2015), pp. 96-103
[40]
M.-L. Zhu, D.-Q. Wang, F.-Z. Xuan
Effect of long-term aging on microstructure and local behavior in the heat-affected zone of a Ni–Cr–Mo–V steel welded joint
Mater. Char., 87 (2014), pp. 45-61
[41]
W. Elber
Fatigue crack closure under cyclic tension
Eng. Fract. Mech., 2 (1) (1970), pp. 37-45
[42]
L.G. Zhao, J. Tong, J. Byrne
The evolution of the stress‐strain fields near a fatigue crack tip and plasticity‐induced crack closure revisited
Fatigue Fract. Eng. Mater. Struct., 27 (1) (2010), pp. 19-29
[43]
R. Pippan, A. Hohenwarter
Fatigue crack closure: a review of the physical phenomena
Fatigue Fract. Eng. Mater. Struct., 40 (4) (2017), pp. 471-495
[44]
R. Pippan, G. Strobl, H. Kreuzer, C. Motz
Asymmetric crack wake plasticity – a reason for roughness induced crack closure
Acta Mater., 52 (15) (2004), pp. 4493-4502
[45]
M. Mokhtarishirazabad, P. Lopez-Crespo, B. Moreno, A. Lopez-Moreno, M. Zanganeh
Optical and analytical investigation of overloads in biaxial fatigue cracks
Int. J. Fatigue, 100 (2017), pp. 583-590
[46]
P.F.P. de Matos, D. Nowell
Experimental and numerical investigation of thickness effects in plasticity-induced fatigue crack closure
Int. J. Fatigue, 31 (11) (2009), pp. 1795-1804

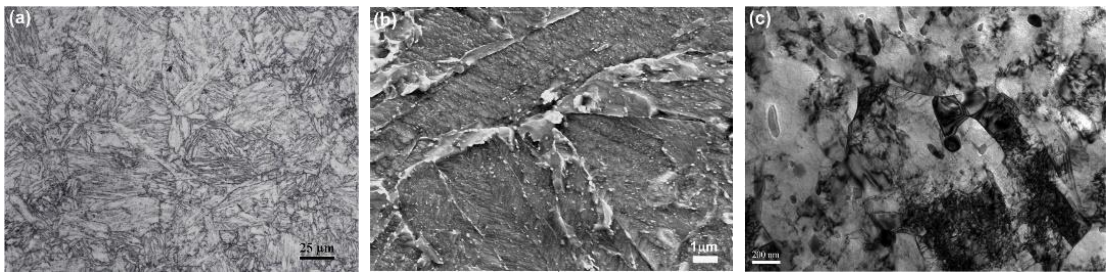

Fig. 1 OM (a), SEM (b) and TEM (c) images showing microstructures of FQTZ in HAZ of the welds [34].

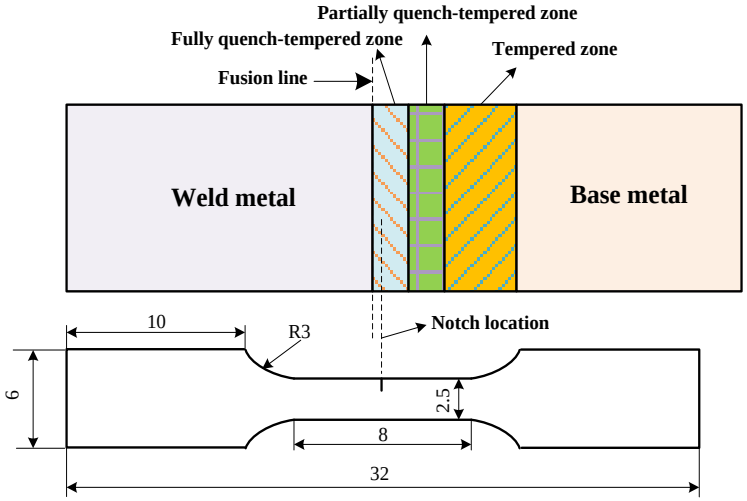

Fig. 2 Shape, dimensions and location of the miniature specimen for in-situ fatigue test.

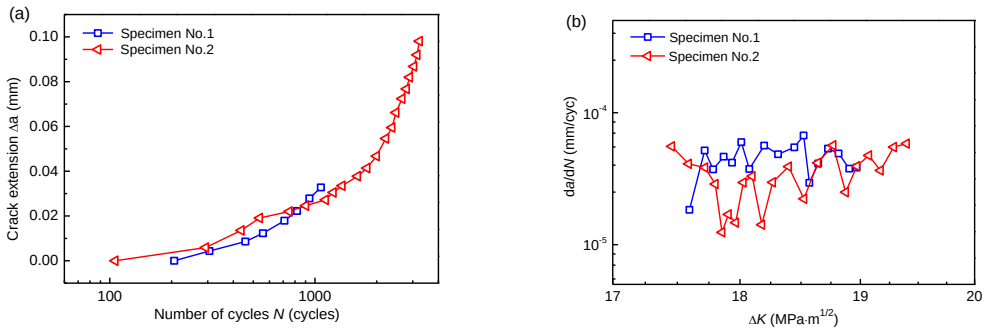

Fig. 3 Short fatigue crack growth behavior: (a) Δa–N relationship, (b) da/dN–ΔK relationship [34].

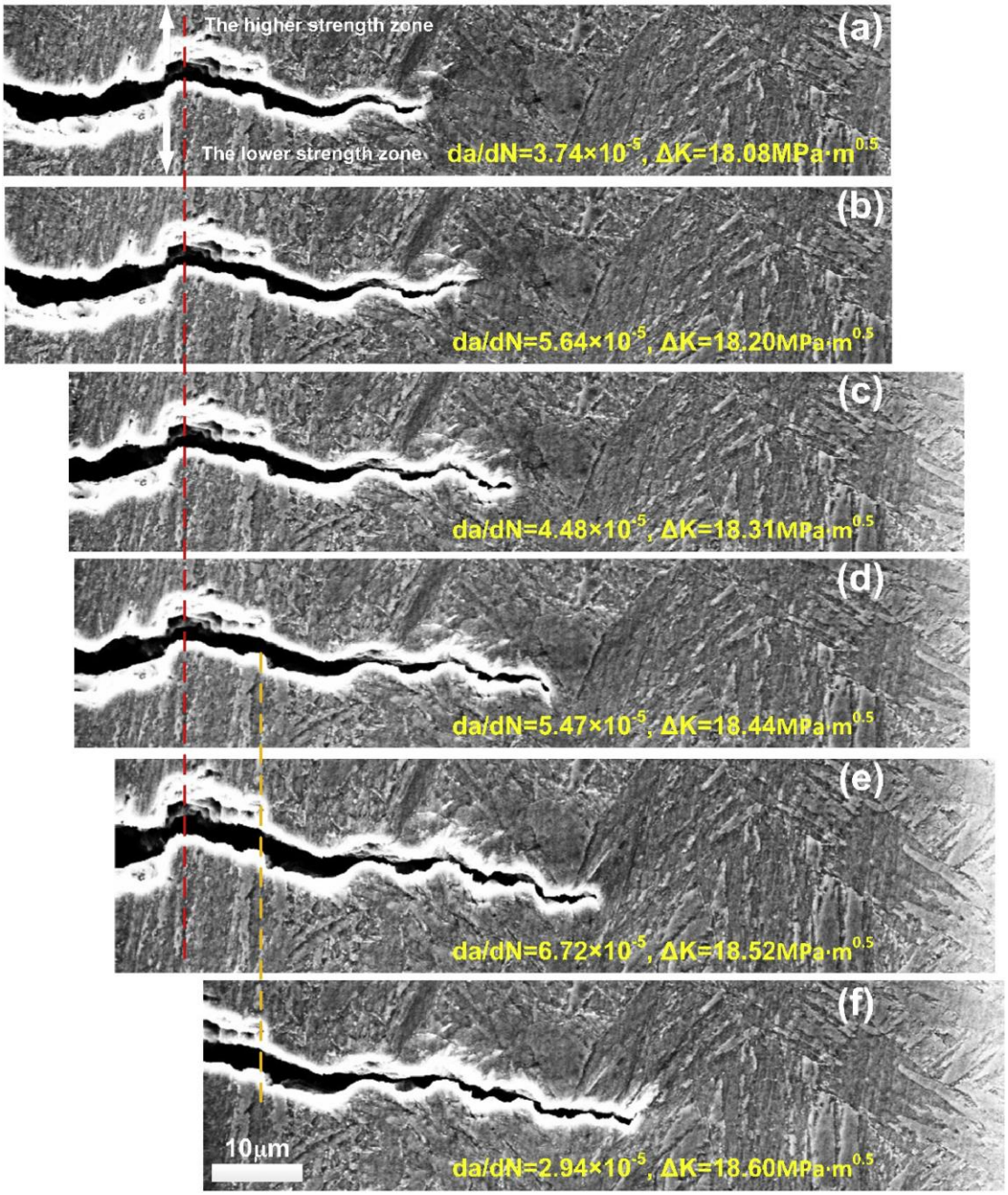

Fig. 4 Morphologies of short fatigue crack growth path in specimen No.1: (a) $a = 0.5176$ mm, $N = 458$ cycles, (b) $a = 0.5213$ mm, $N = 558$ cycles, (c) $a = 0.5269$ mm, $N = 710$ cycles, (d) $a = 0.5312$ mm, $N = 818$ cycles, (e) $a = 0.5369$ mm, $N = 940$ cycles, and (f) $a = 0.5418$ mm, $N = 1069$ cycles (images shown here are taken by holding at P_{max}).

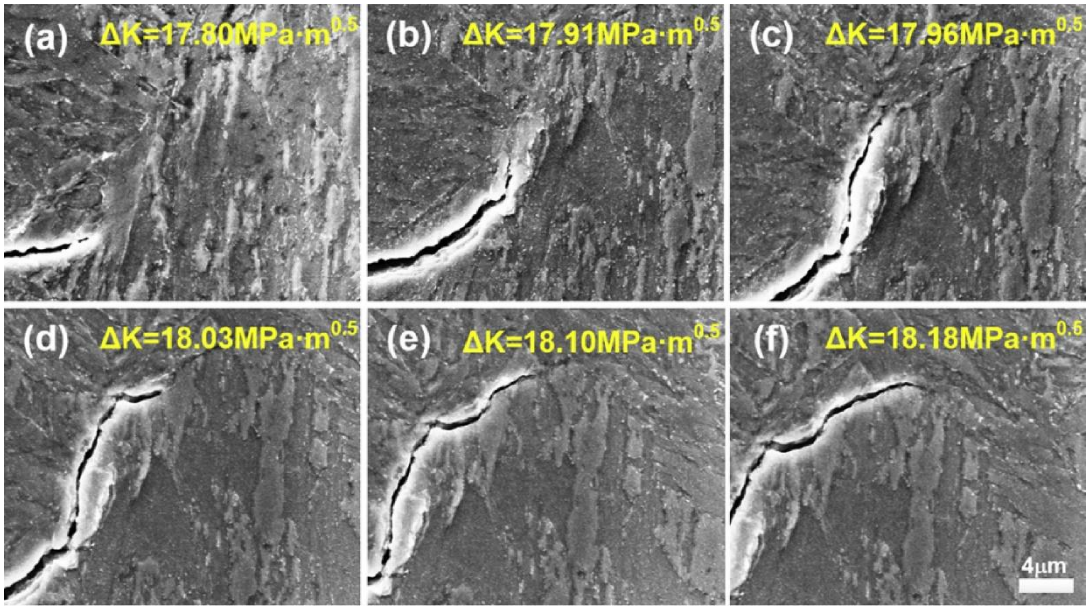

Fig. 5 Morphologies of short fatigue crack growth path in specimen No.2: (a) a=0.698 mm, N=537 cycles; (b) a=0.7032 mm, N=902 cycles; (c) a=0.7065 mm, N=1126 cycles; (d) a=0.7095 mm, N=1228 cycles; (e) a=0.7138 mm, N=1357 cycles; (f) a=0.7174 mm, N=1613 cycles (images shown here are taken by holding at P_{max}).

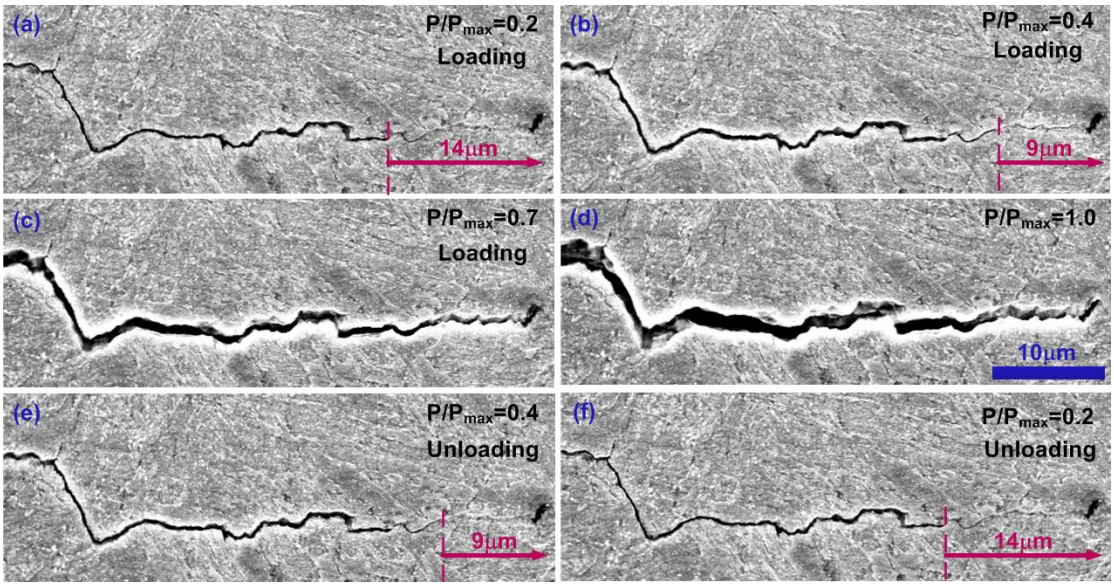

Fig. 6 Development of crack surface contact in a full cycle (specimen No.2) at selected P/P_{max} levels with ΔK of 19.45 MPa·m$^{1/2}$: loading part from (a) to (c), maximum load (d), and unloading part (e) and (f). All images have the same scales as the one shown in (d).

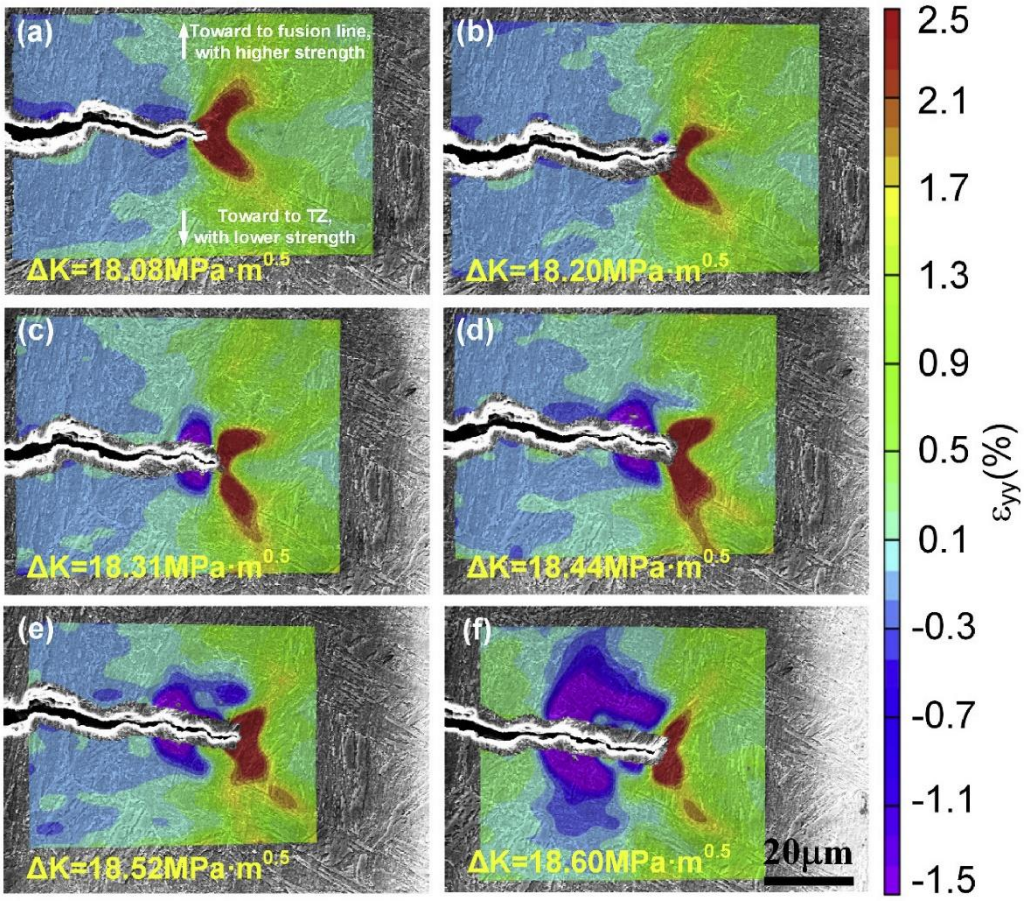

Fig. 7 Strain evolution near crack-tip during short crack growth process (specimen No.1): a, N and ΔK values at (a)–(f) are the same to those in Fig. 4.

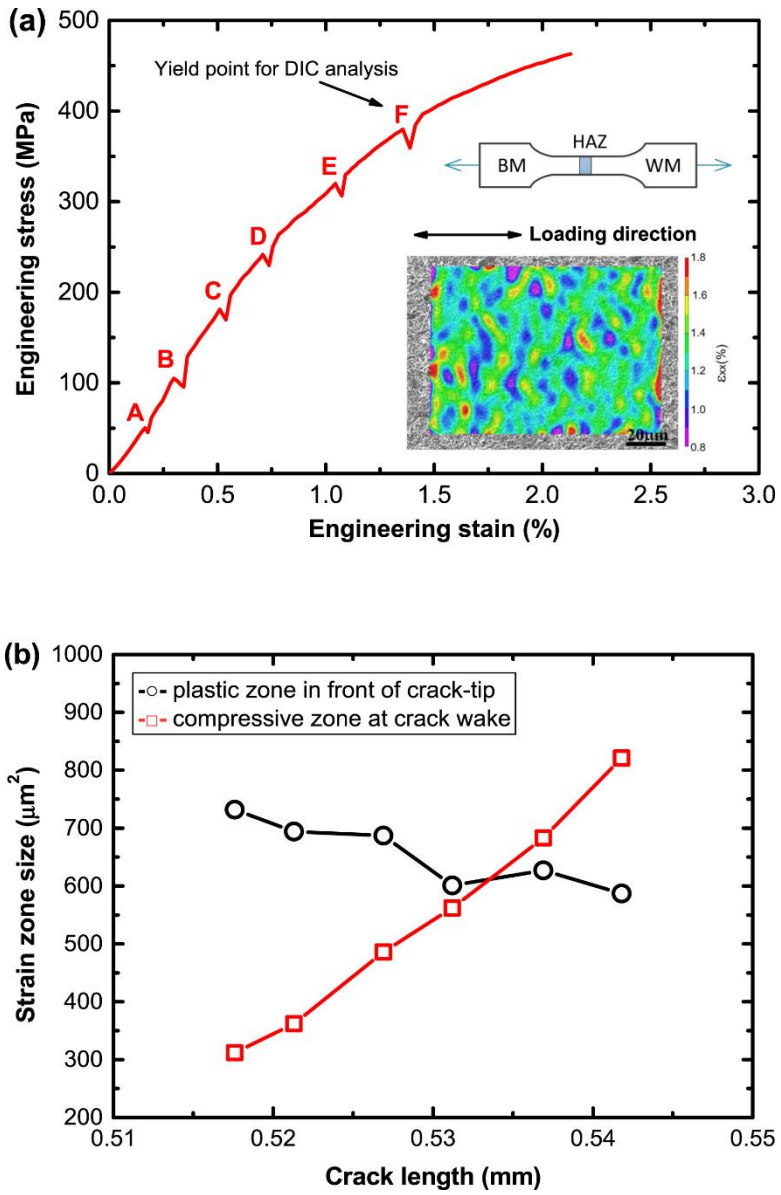

Fig. 8 Quantitative representation of strain evolution near crack-tip and at crack wake in Fig. 7: (a) engineering stress-strain relationship of the miniature sample for plastic strain determination, (b) the evolution of compressive straining area and crack-tip plastic straining area.

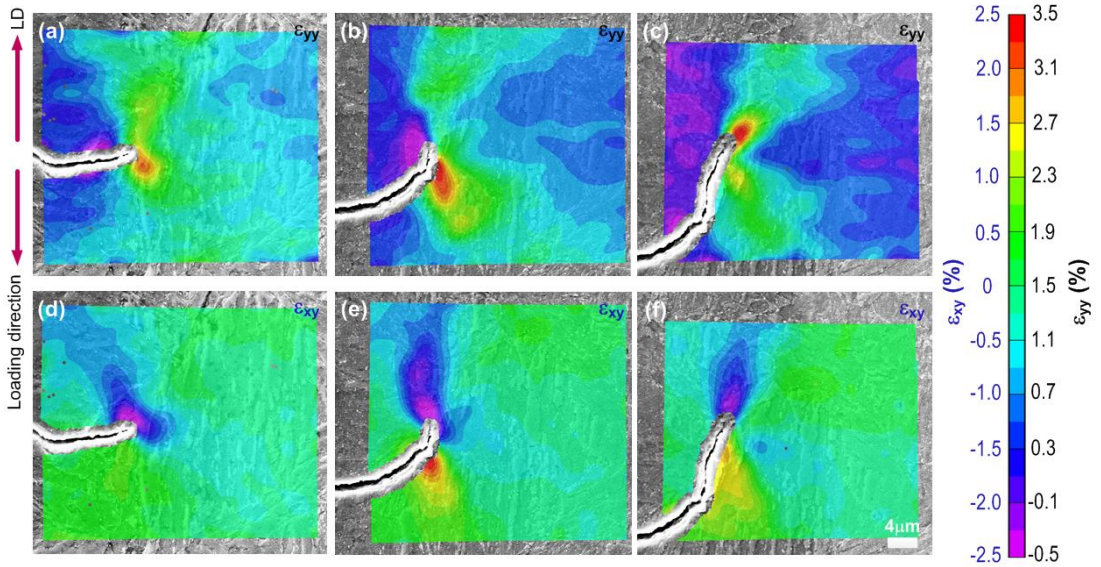

Fig. 9 Evolution of strain components ε_{yy} (a-c) and ε_{xy} (d-f) near crack-tip during deflection of crack growth path (specimen No.2).

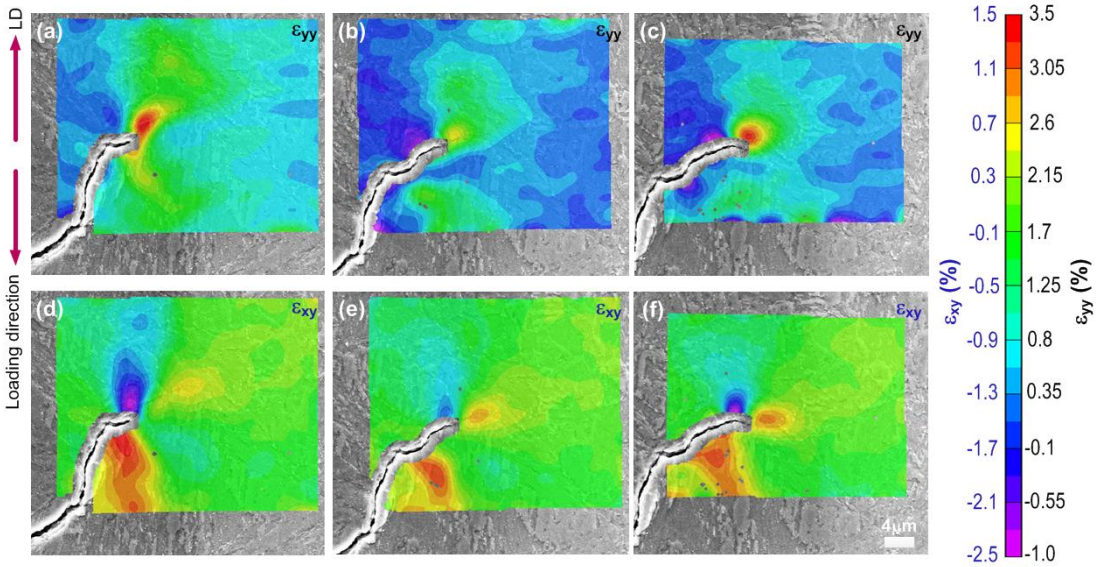

Fig. 10 Evolution of strain components ε_{yy} (a-c) and ε_{xy} (d-f) near crack-tip for intergranular crack growth (specimen No.2).

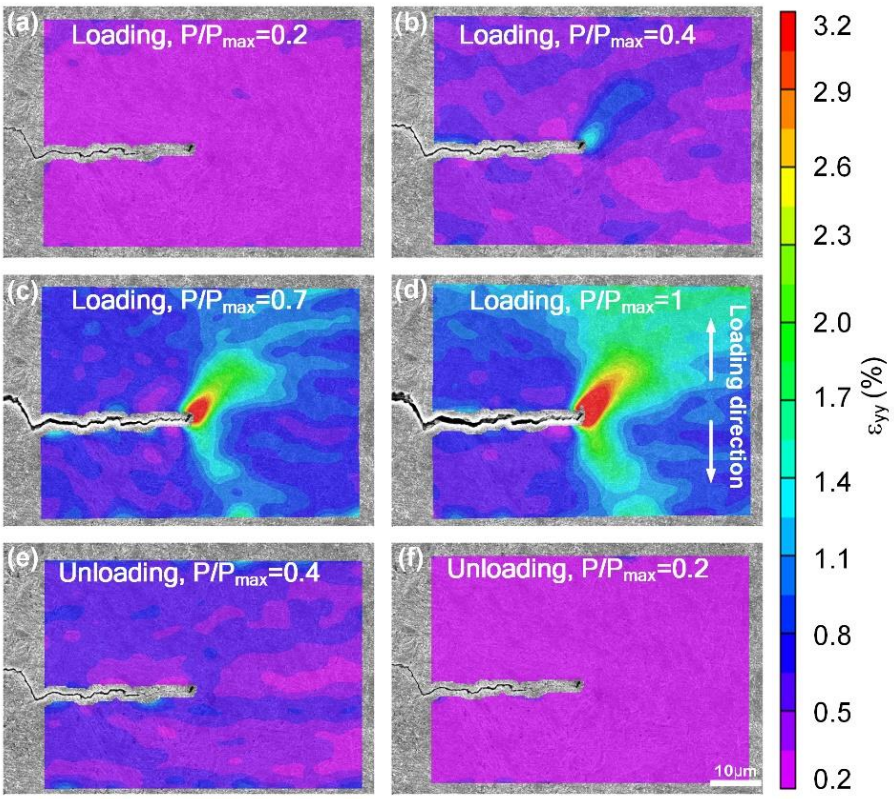

Fig. 11 Strain evolution at final crack-tip within a full cycle at the ΔK of 19.45 MPa·m$^{1/2}$.

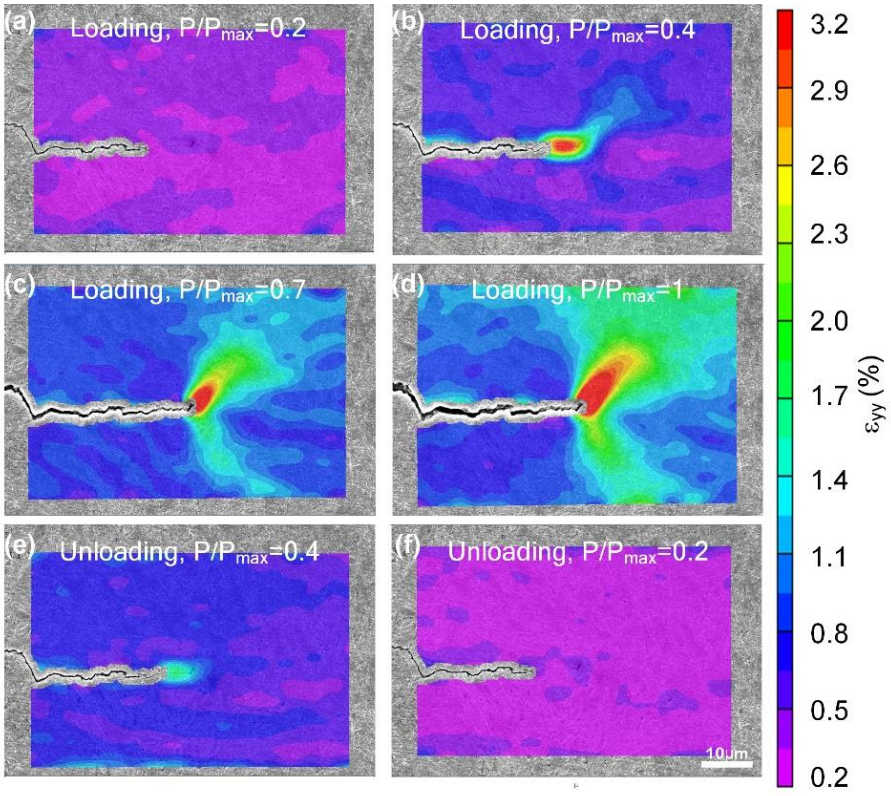

Fig. 12 Strain evolution at instant crack-tip within a full cycle at the ΔK of 19.45 MPa·m$^{1/2}$.

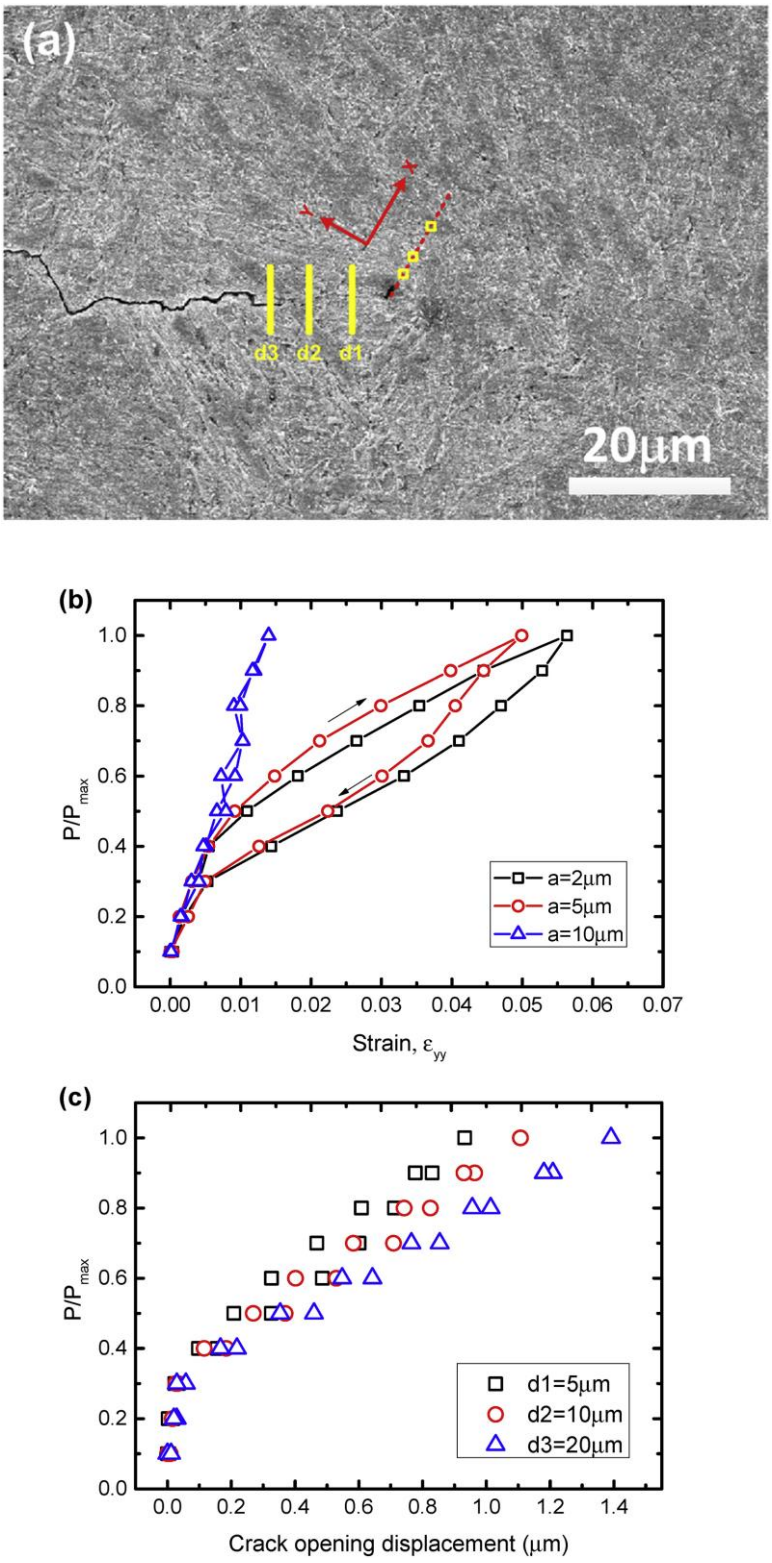

Fig. 13 Variations of strain values in front of crack-tip and COD at the crack wake in a full cycle

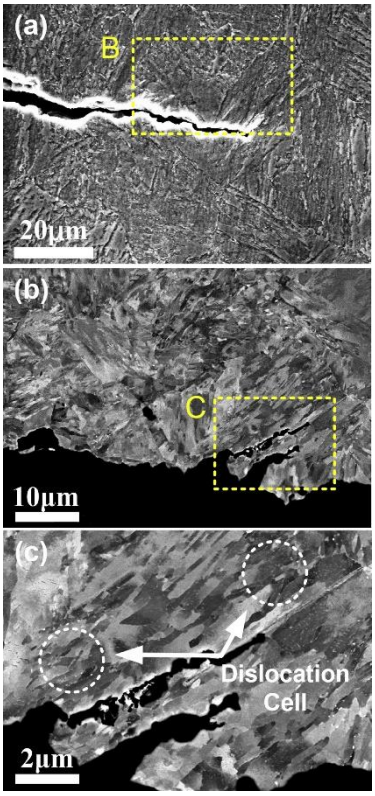

Fig. 14 ECC images of crack growth path of the specimen No.1: (a) an overall view of crack growth path, (b and c) enlarged views of selected areas.

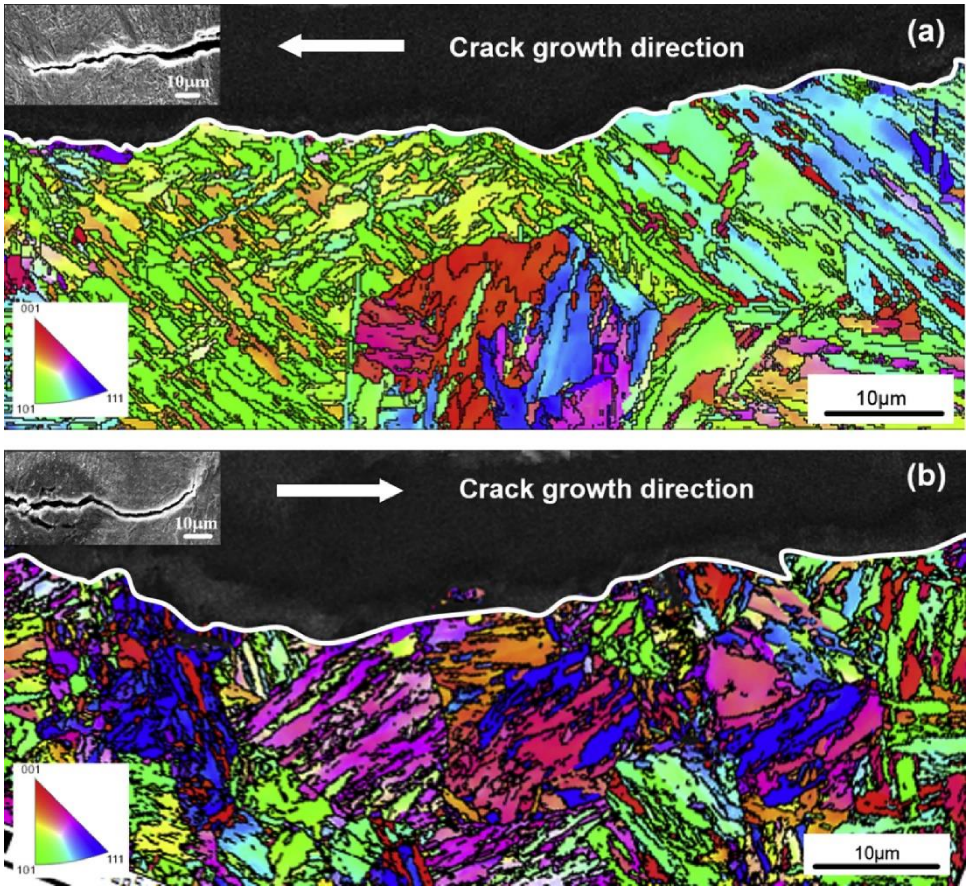

Fig. 15 EBSD observation of fatigue crack growth: (a) IPF-Z map of crack-tip zone of specimen No.1, (b) IPF-Z map of crack growth deflection of specimen No.2 (the arrows show the crack growth direction and the white lines indicate crack growth paths).

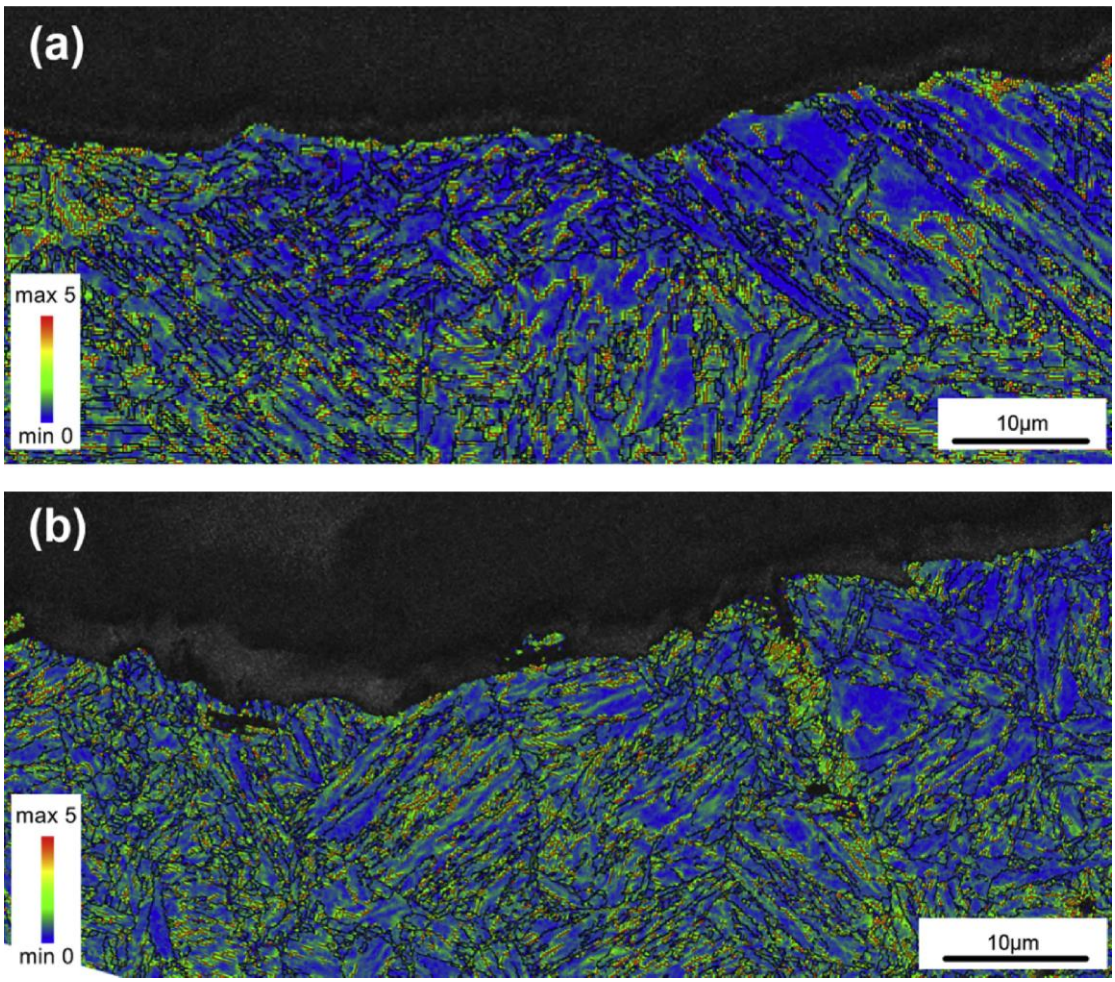

Fig. 16 The corresponding KAM maps resulted from EBSD analyses: (a) crack-tip zone of specimen No.1, (b) crack path deflection zone of specimen No.2.